





RKKY-type in-plane ferromagnetism in layered $\text{Mn}_{1/4}\text{NbS}_2$ single crystalsAzizur Rahman,^{1,*} Majeed Ur Rehman,^{2,*} Muhammad Yousof,¹ Maryam Kiani,² Hongze Zhao,¹ Jianlin Wang ,^{3,4} Yalin Lu,^{3,4} Keqing Ruan,^{1,5} Rucheng Dai,⁶ Zhongping Wang ,⁶ Wei Liu,^{7,†} Lei Zhang ,^{8,‡} and Zengming Zhang ^{6,5,§}¹*Department of Physics, University of Science and Technology of China, Hefei 230026, China*²*College of Physics and Optoelectronic Engineering, Shenzhen University, Nanshai Ave 3688, Shenzhen, Guangdong 518060, People's Republic of China*³*Hefei National Research Center for Physical Sciences at the Microscale, University of Science and Technology of China, Hefei 230026, China*⁴*Anhui Laboratory of Advanced Photon Sciences and Technology, University of Science and Technology of China, Hefei 230026, China*⁵*Key Laboratory of Strongly-Coupled Quantum Matter Physics, Chinese Academy of Sciences,**School of Physical Sciences, University of Science and Technology of China, Hefei, Anhui 230026, China*⁶*The Centre for Physical Experiments, University of Science and Technology of China, Hefei 230026, China*⁷*Institutes of Physical Science and Information Technology, Anhui University, Hefei 230601, China*⁸*High Magnetic Field Laboratory, Hefei Institutes of Physical Science, Chinese Academy of Sciences, Hefei 230031, China*

(Received 22 February 2022; revised 14 May 2022; accepted 25 May 2022; published 8 June 2022)

Placing the layers of the $3d$ magnetic elements in the van der Waals gap pulls the Nb/Ta-based transition metal dichalcogenides family from a nonmagnetic to a magnetic zone. However, the magnetic spectrum is strongly sensitive to the specific combination of host lattice and type of intercalated magnetic element and thus each combination needs a proper explicit study. In this context, we systematically investigate the magnetization of the Mn-intercalated layered ferromagnet $\text{Mn}_{1/4}\text{NbS}_2$ single crystal. Magnetization measurement revealed paramagnetic to ferromagnetic phase transition at around 105 K and an easy in-plane ($H \perp c$) significantly high magnetic anisotropy. The in-plane magnetic anisotropic energy (MAE) evaluated via the noncollinear first-principle approach is $\sim -600 \mu\text{eV}$ per unit cell. The position of the Fermi level in between the spin-up and spin-down Mn states suppresses the positive contribution in the overall MAE, which lifts the overall MAE negative (in plane) with a larger size in $\text{Mn}_{1/4}\text{NbS}_2$. The comprehensive analysis of magnetization isotherms measured in the vicinity of T_c with magnetic field H applied parallel to the ab plane ($H \perp c$) yields the asymptotic critical exponents $\beta = 0.3251(2)$ and $\gamma = 1.2(1)$, and $\delta = 4.691(1)$. These critical exponents fulfill the scaling relation and scaling equation of the magnetic state predicted by the scaling theory. The determined critical exponents agree well with those obtained from the results of the renormalization group theory approach for a three-dimensional Ising system coupled with a long-range interaction between spins decaying as $J(r) \approx r^{-(d+\sigma)}$ with $\sigma = 1.84$. The Ising-type spin state in $\text{Mn}_{1/4}\text{NbS}_2$ is attributed to the higher size of MAE. Our theoretical analysis shows that indirect exchange interaction between Mn-Mn along the c axis, mediated via spins' polarized conduction electrons of Nb atoms, a Ruderman-Kittel-Kasuya-Yoshida (RKKY) type ferromagnetic interaction, dominates over the direct in-plane Mn-Mn exchange interaction (less favorable due to large $d_{\text{Mn-Mn}} \sim 6.67 \text{ \AA}$) and is thus responsible for the macroscopic magnetization in $\text{Mn}_{1/4}\text{NbS}_2$. The RKKY-type ferromagnetic interaction in $\text{Mn}_{1/4}\text{NbS}_2$ arises due to the large spin polarization of the conduction electrons associated with the Nb atoms at the Fermi energy and existence of unoccupied Mn $3d$ states well above the Fermi level.

DOI: [10.1103/PhysRevB.105.214410](https://doi.org/10.1103/PhysRevB.105.214410)**I. INTRODUCTION**

Transition-metal dichalcogenides (TMDCs) have been the subject of various scientific investigations for many years since they exhibit a broad spectrum of structure- and composition-dependent properties. Despite being nonmagnetic themselves, some of the well-known TMDC materials allow insertion [1] of magnetic $3d$ elements and have a

tendency to form ordered compounds, which creates a family of TMDC-based magnetic compounds exhibiting novel magnetic and transport properties. In particular, the ternary $3d$ transition-metal intercalations of niobium and tantalum dichalcogenides, $T_x\text{MX}_2$ ($T = \text{V, Cr, Mn, Fe, Co, Ni}$; $M = \text{Nb, Ta}$; $X = \text{S, Se}$; $x = 1/4, 1/3$), attracted significant interest due to their diverse magnetic [2–5], structural characteristics, and strong spin orbital coupling. Owing to their fascinating characteristics, $T_x\text{MX}_2$ systems have been extensively researched both theoretically and experimentally. Many interesting phenomena have been observed, such as chiral magnetic nanostructures, one-dimensional (1D) nontrivial magnetic solitons, three-state nematic ordering, reversible resistivity switching, sizable bulk Dzyaloshinskii-Moriya

*These authors contributed equally to this work.

†Corresponding author: liuwei@ahu.edu.cn

‡Corresponding author: zhanglei@hmf.ac.cn

§Corresponding author: zzm@ustc.edu.cn

interaction (DMI), and giant topological Hall resistivity. Benefitting from the layered crystal structure, T_xMX_2 can be exfoliated down to 2D scale. Hence T_xMX_2 compounds are expected to provide unique features to the emerging fields of 2D spintronics and soliton physics.

On the other hand, the magnetic properties, such as the direction of the easy axis of magnetization, the field dependence of the magnetization of the ferromagnetic (FM) intercalations, the anisotropy of the paramagnetic susceptibility, and the size of the effective magnetic moment, are strongly dependent on the intercalate ion but relatively insensitive to the host [3]. Due to the large in-plane separation among the intercalant ions, indirect exchange interactions such as superexchange (via the orbitals on the chalcogen ions within the layers) and Ruderman-Kittel-Kasuya-Yoshida (RKKY) interactions (mediated through the conduction electrons) have previously been proposed to be important in these systems. The nature of these indirect interactions, however, is sensitive to the intercalant choice and content [3]. Thus, depending on the stoichiometry of the intercalant, this family offers both antiferromagnetic (AFM) and FM layered features. For example, $Co_{1/3}NbS_2$ and $Fe_{1/3}NbS_2$ [6] are AFM [7], whereas $V_{1/3}NbS_2$ is a ferromagnet with an easy-plane anisotropy [3]. $Cr_{1/3}NbS_2$ has been identified as a helimagnet that exhibits a chiral soliton lattice when a magnetic field is applied in the ab plane [8,9]. The formation of helimagnetic order in $Cr_{1/3}NbS_2$ and $Mn_{1/3}NbS_2$ confirms the strong coupling between neighboring layers, which is consistent with its 3D Heisenberg type spin interaction [10–12]. Fe_xTaS_2 ($x = 1/4, 1/3$) is the only member of this family that has FM order and a strongly c -axis-aligned magnetic easy axis, which is similar to the recently discovered 2D magnets [13–16]. A critical behavior analysis in $Fe_{1/4}TaS_2$, around the paramagnetic to ferromagnetic (PM-FM) transition revealed a Heisenberg type spin interaction [17]. However, our recent comprehensive magnetic study of $Fe_{1/3}TaS_2$ single crystals realized the spin interaction of a (2D)-Ising type. Therefore, the sensitivity of the physical properties to composition (the nature of the intercalated $3d$ metal) and stoichiometry in this class of materials, i.e., T_xMX_2 , yields versatile magnetic systems. The magnetic behavior of this family of compounds cannot be generalized from the behavior of a single compound, and further research is needed on these compounds. Understanding the magnetic mechanisms in these systems is crucial for practical application of these materials in device applications. The analysis of the critical exponents associated with the PM-FM transition is an effective method for identifying the magnetic mechanism and properties.

The current study focuses on the magnetic characteristics of Mn-inserted 2H-NbS₂ with a manganese concentration of 25%. In this specific concentration, the bulk inversion symmetry of the crystal remains intact, preventing the possibility of asymmetric interaction (DM interaction). The nature of the spin coupling, as experimentally investigated by a critical behavior analysis in the vicinity of the PM-FM transition, was found to be consistent with the theoretical prediction of the (3D)-Ising model. To gain a deeper understanding of spin interaction and to interpret the details of the experimental observations, we used theoretical simulations based on density functional theory (DFT) calculations, which revealed that

coupling between further neighbor spins in $Mn_{1/4}NbS_2$, mediated by long-range RKKY interaction, stabilizes FM ordering in the Ising-spin state.

II. RESULTS AND DISCUSSION

A. Experimental details

$Mn_{1/4}NbS_2$ single crystals were grown via the chemical vapor transport method using iodine as the transport agent [18]. Energy dispersive x-ray (EDX) spectrometry was used to carefully investigate the chemical compositions. X-ray diffraction (XRD) (Rigaku SmartLab) with Cu K_α radiation was used to study the structure and phase purity of $Mn_{1/4}NbS_2$. Single-crystal x-ray diffraction measurements were performed on crystalline samples of $Mn_{1/4}NbS_2$ using a Super Nova, Dual, Cu, AtlasS2 diffractometer. An incident x-ray beam with wavelength Mo K_α ($\lambda = 0.71073 \text{ \AA}$) was used. The measured samples had dimensions $\sim 0.15 \text{ mm} \times 0.12 \text{ mm} \times 0.11 \text{ mm}$. Reflections were collected at room temperature over a 2θ range of 7.05° to 58.6° with a resolution of $\sim 0.6 \text{ \AA}$. Using Olex2 [19], the structure was solved with the SHELXS [20] structure solution program using direct methods and refined with the SHELXL [21] refinement package using least squares minimization. A Quantum Design superconducting quantum interference device with vibrating sample magnetometer was used to measure magnetization. To guarantee a precise magnetic field, the no-overshoot mode was used. Before the data was collected, the magnetic field was relaxed for two minutes. The sample was heated to the target temperature above T_c for 10 min before being cooled to the target temperature under a zero magnetic field to measure the initial isothermal magnetization.

B. Structural properties

The crystal structure of $Mn_{1/4}NbS_2$ is illustrated in Fig. 1(a). The NbS₂ is a quasi-two-dimensional system with van der Waals interaction between the layers. Mn atoms are intercalated in the octahedral gaps between the 2H-NbS₂ trigonal prismatic layers [22]. Figure 1(b) gives the chemical ratio obtained by the EDX spectrum. The chemical composition was calculated and compared to the integrated intensity ratios of individual elemental peaks. The average of the three areas results in a $Mn_{0.25(7)}NbS_{1.96(3)}$ composition, which is very close to the ideal $Mn_{1/4}NbS_2$ composition. Figure 1(c) depicts the XRD pattern of $Mn_{1/4}NbS_2$ single crystal; only (00 l) peaks were observed, indicating that the crystal surface is normal to the c axis and its plate-shaped surface is parallel to the ab plane. A series of strong sharp diffraction peaks are consistent with recent studies [23] and JCPDS No. 22-0360. The single peak and narrow FWHM (0.077) of the rocking curve depicted in the inset of Fig. 1(c) demonstrate the high quality of the single crystal sample without any misoriented blocks or twin crystal. To obtain the refined crystal structure and related lattice parameters, single crystal XRD is performed, and the diffraction pattern is refined. The results are shown in Table I. The obtained structural parameters agree with previous reports [23].

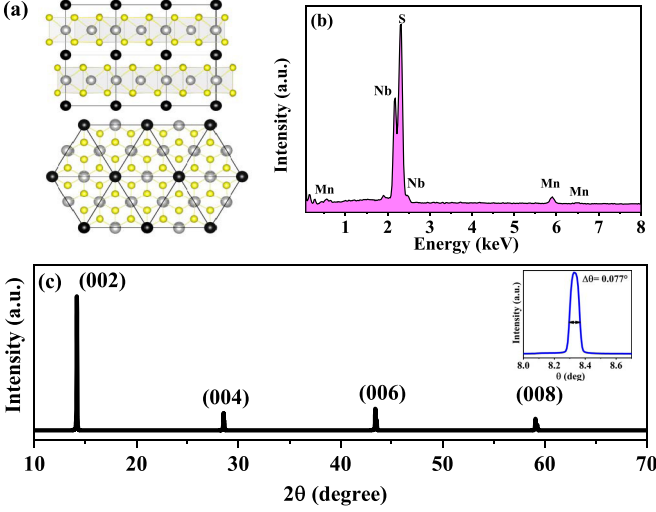


FIG. 1. (a) Crystal structure of $\text{Mn}_{1/4}\text{NbS}_2$, which consists of alternate stacking of NbS_2 layers where the Mn atoms are intercalated between NbS_2 layers [both top view (up) a side view (down)]. Filled sphere black, gray, and yellow represent Mn, Nb, and S, respectively; (b) a typical EDX spectrum for single-crystal $\text{Mn}_{1/4}\text{NbS}_2$; (c) single crystal XRD pattern of $\text{Mn}_{1/4}\text{NbS}_2$ at room temperature. The observed sharp (00 l) peaks imply the high quality of $\text{Mn}_{1/4}\text{NbS}_2$ single crystal [the x-ray rocking curves from the reflection of (002) peak].

C. Magnetization

Figure 2(a) illustrates the temperature dependent magnetization $M(T)$ for applied magnetic fields $H \parallel c$ and $H \perp c$ using zero field cooled (ZFC) and field cooled (FC) sequences. When the temperature increases, one can observe the apparent FM-PM transitions from both field configurations. However, the magnetization values of $H \perp c$ are significantly higher than those of $H \parallel c$, indicating that the easy magnetization direction is within the ab plane. The FM-PM phase transition temperature is estimated to be 105.7 K based on the minimal point of the dM/dT of ZFC curve ($H \perp c$) shown in the inset of Fig. 2(a). Figure 2(b) shows the isothermal magnetization measured at $T = 5$ K. The observed saturation moment of Mn ions is approximately $3.99\mu_B/\text{f.u.}$. As illustrated in the left insets of Fig. 2(b), the $M(H)$ curve obtained for $H \perp c$ reflects a typical ferromagnetic character

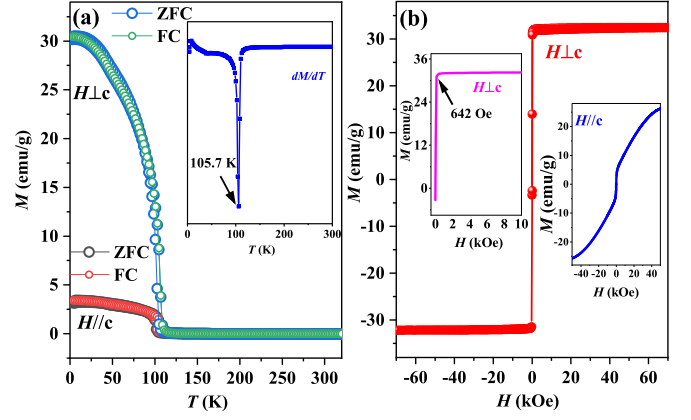


FIG. 2. (a) Temperature dependence of magnetization $M(T)$ measured at 100 Oe for magnetic field $H \perp c$ and $H \parallel c$. The inset shows the derivative magnetization dM/dT vs T of ZFC measurement for $H \perp c$; (b) isothermal magnetization as a function of applied field $M(H)$ at $T = 5$ K with $H \perp c$. The right and left inset show the $M(H)$ loop measured for $H \parallel c$ and $H \perp c$, respectively.

with the saturation field ($H_s^\perp \approx 642$ Oe). However, this behavior does not appear on the $M(H)$ curve for $H \parallel c$, where the magnetization is not saturated until high magnetic field as shown in Fig. 2(b). The $M(H)$ curves realized the significantly high magnetic anisotropy between the ab plane and c axis in $\text{Mn}_{1/4}\text{NbS}_2$.

To characterize the FM-PM transition in $\text{Mn}_{1/4}\text{NbS}_2$, a series of magnetization isotherms [$M(H)$] are measured along the $H \perp c$ and the $H \parallel c$ as shown in Fig. 3(a) and Fig. 3(b), respectively. The [$M(H)$] curves measured for $H \perp c$ show a typical saturation behavior, whereas the [$M(H)$] curves for $H \parallel c$ do not saturate even at high fields; thus the critical behavior analysis is performed for $H \perp c$. According to the Landau theory of phase transition, the Gibbs free energy $G(T, M)$ for a magnetic system in the vicinity of the phase transition can be expressed as [24]

$$G(T, M) = G_0 + a \frac{T - T_c}{T_c} M^2 + bM^4 - MH, \quad (1)$$

where a and b are the Landau coefficients. $G(T, M)$ enables us to determine the nature of the phase transition around T_c . The minimization of the thermodynamic potential ($\partial G/\partial M = 0$) yields the equilibrium condition, resulting in

$$M^2 = \frac{1}{4b} \frac{H}{M} - \frac{a}{2b} \varepsilon, \quad (2)$$

where $\varepsilon = (T - T_c)/T_c$ is the reduced temperature. The M^2 vs H/M curves around T_c form an Arrott plot. According to the Landau mean field model, the $M(H)$ curves plotted as M^2 vs H/M should be a series of straight lines parallel to each other in the high field region [25]. For lines below T_c , the intercept of the M^2 as a function of H/M on the y axis should be positive, while, for lines above T_c , should be negative (i.e., no spontaneous magnetization), whereas, at $T = T_c$, the line should pass through the origin. In addition, the slopes of the straight line can be used to determine the order of phase transition, according to Banerjee's criterion [26]. A positive slope indicates a second-order phase transition, while

TABLE I. $\text{Mn}_{1/4}\text{NbS}_2$ structural information.

Composition	References
Sample	$\text{Mn}_{1/4}\text{NbS}_2$
Temperature/K	293 K
Crystal system	Hexagonal
Space group	$P6_3/mmc$
$a/\text{\AA}$	6.6662(10)
$b/\text{\AA}$	12.454(3)
$\alpha/\text{\AA}$	90
$\gamma/\text{\AA}$	120
Volume/ \AA^3	479.29(18)
Goodness of fit	1.085
R factor	1.71%

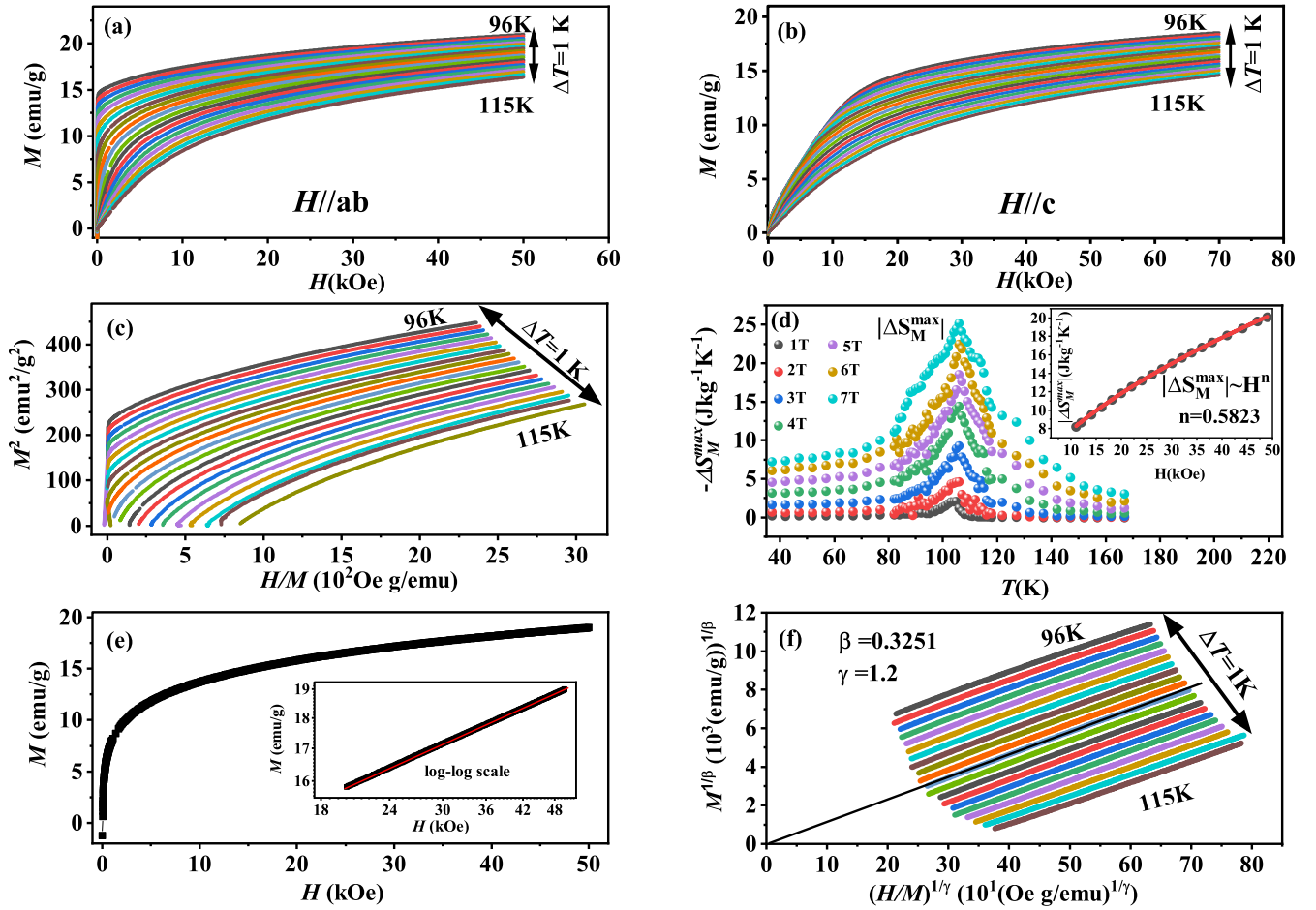


FIG. 3. (a) The magnetic isotherms $M(H)$ around T_c for $H \perp c$; (b) for $H \parallel c$ for $\text{Mn}_{1/4}\text{NbS}_2$; (c) Arrott plots of M^2 vs H/M around T_c for $\text{Mn}_{1/4}\text{NbS}_2$; (d) Temperature dependence of magnetic entropy change $[\Delta S_M(T)]$ under different fields; The inset shows field dependence of the maximum of magnetic entropy change $|\Delta S_M^{\max}|$, i.e. the peak of $-\Delta S_M(T)$ curve (the solid curve is fitted); (e) fitting of $M(H)$ at T_c (inset shows that on log-log scale); (f) modified Arrott plot based on the obtained critical exponents $\beta = 0.3251$ and $\gamma = 1.2$.

a negative slope implies a first-order phase transition. M^2 vs H/M in Fig. 3(c) does not show a series of parallel straight lines, implying that the Landau mean-field theory is invalid for $\text{Mn}_{1/4}\text{NbS}_2$. However, the concave downward curvature of the M^2 vs H/M curves clearly indicates the FM-PM transition in $\text{Mn}_{1/4}\text{NbS}_2$ is of second order.

More universally, M^2 versus H/M fulfills the Arrott-Noakes equation of state in the asymptotic critical region ($|\epsilon| < 0.1$) [27]:

$$(H/M)^{1/\gamma} = (T - T_c)/T_c + (M/M_1)^{1/\beta}, \quad (3)$$

where M_1 is a constant. The parameters β [related with spontaneous magnetization $M_S(T)$] and γ [associated with initial susceptibility $\chi_0^{-1}(T)$] are critical exponents that imply important hints about magnetic interactions, such as correlating length, spin dimensionality, magnetic coupling decaying distance, etc. The $M(H)$ curves plotted as $M^{1/\beta}$ vs $(H/M)^{1/\gamma}$ form the modified Arrott plot (MAP).

In view of the correlation between critical exponents and magnetic entropy change (ΔS_M), the field-dependent (ΔS_M) can be used to determine critical exponents β and γ . The ΔS_M can be calculated from magnetization isotherms around

T_c using Maxwell's relation [28]:

$$\begin{aligned} \Delta S_M(T, H) &= \Delta S_M(T, H) - \Delta S_M(T, 0) \\ &= \int_0^H [\partial M(T, H)/\partial T]_H dH. \end{aligned} \quad (4)$$

Using the $M(H)$ data in Fig. 3(a), a plot of ΔS_M vs T at various applied magnetic fields is constructed, as shown in Fig. 3(d). Each $\Delta S_M(T)$ curve has a peak corresponding to T_c , suggesting that $T_c = 106.5(5)$ K. The maximum of $|\Delta S_M|$ ($|\Delta S_M^{\max}|$) follows the power law as the magnetic field increases [29]:

$$\begin{cases} |\Delta S_M^{\max}| \propto H^n, \\ n = 1 + \frac{\beta-1}{\beta+\gamma}, \end{cases} \quad (5)$$

where $|\Delta S_M^{\max}|$ is regarded as the peak of the $|\Delta S_M(T)|$ curve and n depends on the magnetic state of the sample. The power law fitting of $|\Delta S_M^{\max}|$ with H gives $n = 0.663(5)$, as can be seen in the inset of Fig. 3(d).

The critical exponent δ , which is associated with the critical temperature T_c , can be determined using critical isotherm

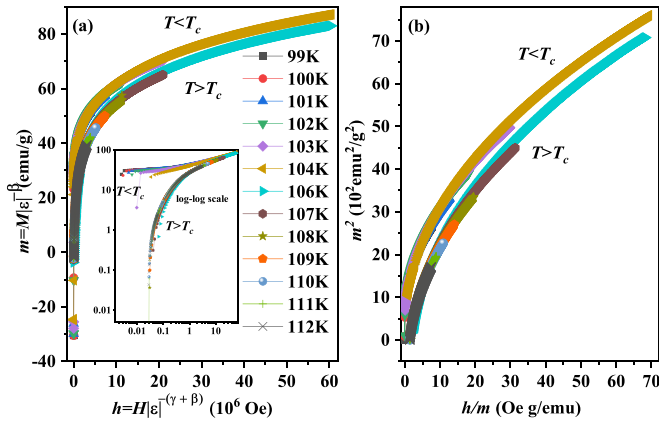


FIG. 4. (a) Scaling plots of renormalized m versus renormalized h around T_c for $M(H)$ at typical temperatures (inset shows the same plot on log-log scale); (b) the renormalized magnetization and field replotted in the form of m^2 vs h/m for $\text{Mn}_{1/4}\text{NbS}_2$.

analysis [30]:

$$M = DH^{1/\delta}, \quad \varepsilon = 0, \quad T = T_c. \quad (6)$$

Figure 3(e) shows the isothermal $M(H)$ at T_c , with an inset displaying the linear fit of the log-log scale in the higher field region. The slope of the linear fit of the log-log plot determines $1/\delta$ and hence $\delta = 4.691(1)$ is obtained. Meanwhile, the critical exponents (β , γ , and δ) should satisfy the Widom scaling relation as follows [31]:

$$\delta = 1 + \frac{\gamma}{\beta}. \quad (7)$$

By combining Eq. (5) and Eq. (7) with the obtained values of δ and n , it can be deduced that $\beta = 0.3251(2)$ and $\gamma = 1.2(1)$. Using these critical exponent values of β and γ , the final modified Arrott plot is constructed as shown in Fig. 3(f). The lines in Fig. 3(f) are all very straight to each other in the high-field region, and the line at $T_c = 105$ K passes through the origin, verifying the reliability of the critical exponents.

To confirm the reliability of these critical exponents as well as T_c , it is necessary to determine whether these critical exponents yield the magnetic equation of state for this system in the asymptotic critical region, which is given below [30]:

$$M(H, \varepsilon) = \varepsilon^\beta f_\pm(H/\varepsilon^{\beta+\gamma}), \quad (8)$$

where f_+ ($T > T_c$) and f_- ($T < T_c$) are the regular functions. By defining the renormalized magnetization $m = M(H, \varepsilon)\varepsilon^{-\beta}$ and renormalized field $h = H\varepsilon^{-(\beta+\gamma)}$ Eq. (8) can be expressed as follows:

$$m = f_\pm h. \quad (9)$$

According to Eq. (9), assuming a proper scaling relation and the correct choice of critical exponents, renormalized m and h will create two separate branches above and below T_c , respectively. Following Eq. (9), the magnetization isotherms around T_c are replotted as m versus h , as shown in Fig. 4(a), while the inset shows the same plot on a log-log scale. It is remarkable that all data for $T > T_c$ and $T < T_c$ collapse into two separate branches. Alternatively, the correctness of

critical exponents and T_c is further verified with a more rigorous method by plotting m^2 vs h/m . Figure 4(b) shows the m^2 vs h/m plot, in which all of the data is observed to collapse into two universal curves: one for $T < T_c$ and another for $T > T_c$. This obviously demonstrates that interactions are properly renormalized in the critical regime using a scaling state equation.

The universality class of a magnetic phase transition for a homogeneous magnet is determined by the exchange interaction $J(r)$. Fisher *et al.* used a renormalization group theory analysis to examine spin interactions. They considered magnetic coupling as an attractive interaction of spins, which results in the exchange distance $J(r)$ decaying with spatial distance r as [31,37]

$$J(r) \approx r^{-(d+\sigma)}, \quad (10)$$

where d denotes spatial dimension and σ is the range of interaction. According to this model, spin interactions are either long or short range, based on the values of $\sigma < 2$ and $\sigma > 2$, respectively, and the susceptibility exponent γ is predicted as follows:

$$\gamma = 1 + \frac{4}{d} \left(\frac{n' + 2}{n' + 8} \right) \Delta\sigma + \frac{8(n' + 2)(n' - 4)}{d^2(n' + 8)^2} \times \left[1 + \frac{2G(\frac{d}{2})(7n' + 20)}{(n' - 4)(n' + 8)} \right] \Delta\sigma^2, \quad (11)$$

where $\Delta\sigma = (\sigma - \frac{d}{2})$, $G(\frac{d}{2}) = 3 - \frac{1}{4}(\frac{d}{2})^2$, and n' represents the spin dimensionality. In order to determine lattice dimensionality (d), spin dimensionality n' , and the range of interactions in $\text{Mn}_{1/4}\text{NbS}_2$, a procedure similar to Ref. [38] was used, where the parameter in the above expression is adjusted for specific values of $\{d : n'\}$ so that it provides a value for close to that found experimentally, $\gamma = 1.2(1)$. The resulting exponent was then used to derive the additional exponents using the following relationships: $v = \gamma/\sigma$, $\alpha = 2 - vd$, $\beta = (2 - \alpha - \gamma)/2$, and $\delta = 1 + \gamma/\beta$. The procedure was carried out with different sets of $\{d : n'\}$. It was found that, for $\{d : n'\} = \{3 : 1\}$ and $\sigma = 1.84(6)$, we obtained the experimentally estimated value of $\gamma = 1.2$. It gives the exponents $\beta = 0.3748(1)$ and $\delta = 4.22(6)$, both of which are well consistent with our experimentally obtained values, which are listed in Table II. Some other related compounds are also listed for comparison. This calculation indicates that the spin interaction in $\text{Mn}_{1/4}\text{NbS}_2$ is of 3D-Ising type coupled with long range ($\sigma = 1.84$) interaction. However, for $\sigma = 1.84$, the value of $\beta = 0.3748$, provided by scaling relations, clearly deviated from the 3D Ising value towards the mean-field value. The value of σ indicates the extended nature of the exchange interaction, which might be attributed to the interactions between spins involving itinerant electrons [39]. In principle, two types of exchange interactions, direct or indirect, can be involved to establish macroscopic magnetization in $\text{Mn}_{1/4}\text{NbS}_2$. However, due to large in-plane separation (~ 6.67 Å) of the Mn-Mn ions in $\text{Mn}_{1/4}\text{NbS}_2$, the direct exchange interaction is less favorable, because the overlapping of Mn $3d$ states referring to different atoms at such large separation is less significant. In $\text{Mn}_{1/4}\text{NbS}_2$, the significant interlayer coupling, in addition to the large Mn-Mn spatial separation, favors the indirect exchange interaction. The

TABLE II. Comparison of critical exponents of $\text{Mn}_{1/4}\text{NbS}_2$ with different theoretical models and related materials.

Composition	References	Technique	β	γ	δ
$\text{Mn}_{1/4}\text{NbS}_2$	This work	MAP	0.325(1)	1.2(1)	4.691(1)
$\text{Fe}_{1/4}\text{TaS}_2$	[17]	MAP	0.460(4)	1.216(11)	3.64(3)
$\text{Cr}_{1/3}\text{NbS}_2$	[10]	MAP	0.370(4)	1.380(2)	4.853(6)
$\text{Mn}_{1/3}\text{NbS}_2$	[12]	MEC	0.3681(1)	1.3917(2)	4.7805(7)
2D Ising	[32]	KF	0.537(2)	1.255(3)	3.33(7)
Mean field	[33]	Theory	0.5	1.0	3.0
3D Heisenberg	[26,34]	Theory	0.365	1.386	4.8
3D XY	[26,35]	Theory	0.345	1.316	4.81
3D Ising	[26,35]	Theory	0.325	1.24	4.82
Tricritical mean field	[36]	Theory	0.25	1.0	5

indirect RKKY interaction, which is mediated by conduction electrons associated with the d orbitals on the Nb or Ta atoms, has previously been proposed as the origin of long range ferromagnetism in transition metal intercalated Nb/Ta chalcogenides. On the other hand, a superexchange interaction via the orbitals on the chalcogen ions within the layers could be a second exchange mechanism that may be relevant in these systems. The type and concentration of intercalant in the host dichalcogenides influence the nature and strength of the indirect exchange interaction. To specify the form of indirect magnetic coupling which is responsible for global magnetization in the current system under investigation, $\text{Mn}_{1/4}\text{NbS}_2$, we used the first principle approach.

We performed the spin-polarized DFT calculations using the Vienna *ab initio* simulation package [40]. For the expansion of Hamiltonian in plane wave bases we use cutoff energy 450 eV and, for the integration over the BZ, the Gamma center $10 \times 10 \times 5$ k -point mesh was adopted. We performed the GGA+ U calculations with a Hubbard U value (the Coulomb energy $U = 3$ eV and Hund exchange parameter $J = 0.7$ eV) for the Mn $3d$ electrons [40]. The D_3 -Grimme correction is also adopted to address the van der Waals interaction between the layers [41]. The spin-orbit coupling (SOC) was considered during the searching for the easy magnetization axis.

Specifically, we noticed the following from our spin-polarized calculations. (i) The magnetic moments that reside at each Mn site in the $2a \times 2a$ Mn lattice (when there are no NbS_2 layers in between the Mn layers) are around $5\mu_B$ [see Fig. 5(a)], indicating a Mn^{+2} valency state. (ii) After inserting the NbS_2 layers between the Mn layers, the Mn moment reduces to the value of $4.1\mu_B$ [see Fig. 5(b)], completely consistent with the experiment. This reduction in the Mn magnetic moment is due to the charge transferring from the Mn layers to the NbS_2 layers [see Fig. 5(c)], indicating a strong coupling between the Mn and NbS_2 layers. The Mn- $3d$ majority spin states are filled while the minority spin states are empty and are located away from the Fermi energy [see Fig. 5(d)]. (iii) Interestingly, the Mn layers induce a negative magnetic moment at the Nb (1) ($\sim -0.1\mu_B$) and Nb (2) ($\sim -0.05\mu_B$) sites [see Fig. 5(b)]. The difference in magnetic moments at Nb(1) and Nb(2) sites are due to their different locations with respect to the Mn atom. For instance, the Nb(1) atom shows a high magnetic moment due to its tight coupling with Mn as compared to Nb(2), which is located at an empty site. The opposite magnetic moments at Nb and Mn sites

indicate an AFM coupling between them [see Figs. 5(g) and 5(h)]. The spin polarization of the conduction electrons is also reflected in the density of states of Nb(1) and Nb(2) atoms [see Figs. 5(d) and 5(e)]. The AFM coupling between the Mn and Nb atoms is also evident from the spin-density ρ_{spn} as shown in Fig. 5(g). The spin polarization of the itinerant electrons appears to be one of the important parameters in magnetic characteristic formations. The direction and size of the induced magnetic moment or spin polarization of the conduction electrons with respect to the local moment of the magnetic atoms are key elements to analyzing and classifying ferromagnets.

The spin-polarized free charge density associated with Nb atoms (Nb $5d$ electrons) binds the Mn layers ferromagnetically along the c axis, suggesting an RKKY ferromagnetic exchange interaction in the $\text{Mn}_{1/4}\text{NbS}_2$ [see Figs. 5(g) and 5(h)]. The RKKY exchange term can be written as $J_{\text{RKKY}} \approx V^4 G(E_F)/E_h^2$, where V represents the coupling between the magnetic ion and the conduction electrons in the metal, $G(E_F)$ represents the density of states (DOS) at the Fermi energy, and E_h is the energy needed to promote an electron from the filled $3d$ level to the Fermi energy [42]. This shows that RKKY type interaction strongly depends on the spin polarization of the conduction electrons at the Fermi energy and the position of unoccupied Mn $3d$ with respect to the Fermi level. Analyzing the DOS of Mn and Nb, we can see that the spin polarization of the Nb conduction electrons at the Fermi energy is large and the unoccupied Mn $3d$ states lie well above the Fermi level; thus a RKKY ferromagnetic interaction will be dominating. The above all is completely consistent with our experimental findings. RKKY type interaction has been previously reported for the $\text{Fe}_{1/4}\text{TaS}_2$ system with an out-of-plane easy magnetization axis [39].

Now we ask the following question. Is the easy-plane magnetization, as observed in our experiment, possible to reflect in our DFT calculations? For this, we performed the noncollinear spin-orbit coupling calculations. By setting the magnetic moments ferromagnetically along different angles (measured from the c axis) we noticed that system energy goes down by tilting the spin direction from out-of-plane ($\parallel c$) to the in-plane direction (ab) [see Fig. 5(i)]. This indicates the in-plane easy magnetization (ab) is the ground state and is in complete agreement with the experiment. Using $\text{MAE} = E(\theta) - E(\parallel c)$, where MAE is the magnetic anisotropy, we estimated the size of MAE $\sim -600 \mu\text{eV}$ per unit cell. The

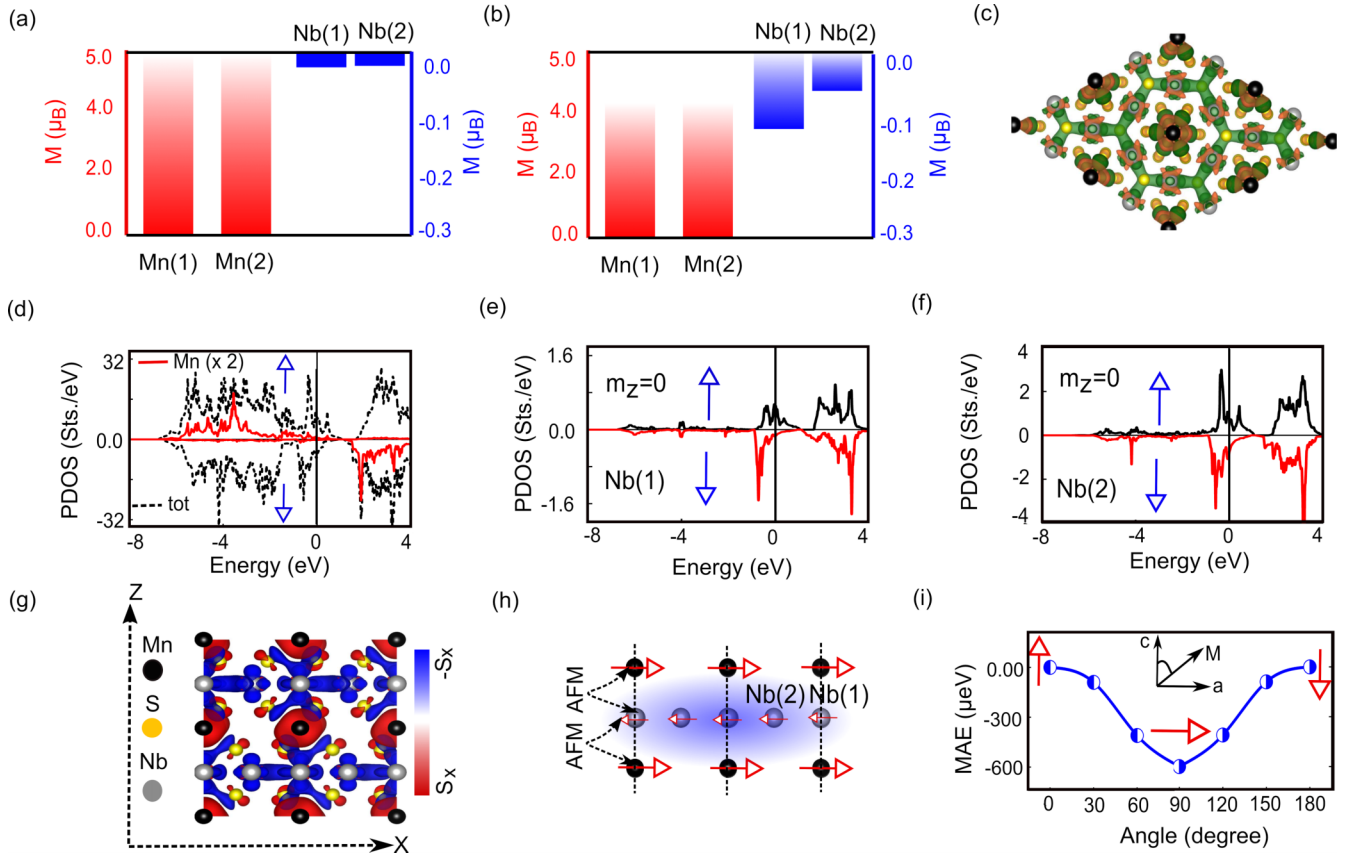


FIG. 5. (a) Magnetic moments of Mn and Nb atoms in a separate $2a \times 2a$ lattice (when there is no coupling between them), where a represents the lattice parameter of mother lattice NbS_2 . (b) Magnetic moments of Mn and Nb atom after insertion of Mn layers in the $2a \times 2a$ lattice of NbS_2 lattice. (c) In plane view of the differential charge density $\rho_c \equiv \rho(\text{Mn}_{1/4}\text{NbS}_2) - \rho(\text{Mn}) - \rho(\text{NbS}_2)$ at the isosurface $\sim 0.0032 e/\text{\AA}^3$. The orange and dark-green colors represent the charge accumulation and charge depletion, respectively. (d) The total spin-up and spin-down charge densities of $\text{Mn}_{1/4}\text{NbS}_2$ together with partial DOS for Mn atom (scaled by the factor of 2). (e),(f) Spin polarized partial DOS projected over the $m_z = 0$ at Nb(1) and Nb(2) sites. (g) Side view of the real space spin density ρ_{spn} at the isosurface $e/\text{\AA}^3$, which visualizes the AFM coupling between Mn and Nb spin moments. (h) Schematic representation showing the AFM coupling between Nb and Mn atoms and FM coupling mediated through the spin polarized conduction electrons. (i) The MAE at different angles θ measured from the c axis. The easy in-plane (ab) magnetization can be noticed.

value of MAE is higher than that of $\text{Mn}_{1/3}\text{NbS}_2$, which is around $-480 \mu\text{eV}$ per unit cell [43]. This increase in MAE is due to the suppression or weakness of the positive MAE term in $\text{Mn}_{1/4}\text{NbS}_2$, which competes with the negative term (in-plane MAE) in the total MAE. The reason involved behind the in-plane easy magnetization can be explained: the DOS of Mn $3d$ states [see Fig. 5(d)] shows that the Fermi level is located between the spin-up and spin-down Mn- d states resulting in a significant SOC induced energy gain associated with the states having opposite spin directions, which competes with the spin diagonal part of the energy (support positive MAE). Due to the considerable value of MAE, the spins in $\text{Mn}_{1/4}\text{NbS}_2$ behave like Ising type as observed in our experiment. Thus $\text{Mn}_{1/4}\text{NbS}_2$ is an RKKY ferromagnet with Ising-type spin states.

III. CONCLUSION

An in-depth investigation of critical phenomena in the quasi-two-dimensional ferromagnet $\text{Mn}_{1/4}\text{NbS}_2$ revealed that the compound undergoes a continuous PM to FM phase tran-

sition at $T_c = 105$ K. The critical exponents $\beta = 0.3251(2)$, $\gamma = 1.2(1)$, and $\delta = 4.691(1)$ determined using magnetic entropy and critical isotherm analysis obey the scaling equation, indicating that the exponents are unambiguous and intrinsic to the material. The obtained critical exponents match well with those determined from the results of the renormalization group theory analysis for a 3D Ising $\{d : n\} = \{3 : 1\}$ system coupled with a long-range spin interaction decaying as $J(r) \approx r^{-(d+\sigma)}$ with $\sigma = 1.84$. The indirect exchange interaction of the RKKY type was noticed to be a dominant contribution and ultimately responsible for the long-range spin interaction in $\text{Mn}_{1/4}\text{NbS}_2$. The appearance of large spin polarization of the Nb conduction electrons and the existence of Mn- $3d$ empty states well above the Fermi level are the two main causes accountable for the RKKY-type dominant contribution in $\text{Mn}_{1/4}\text{NbS}_2$. The easy-plane magnetization was observed as a ground magnetic state while performing both experiment and theoretical DFT calculation. The easy in-plane MAE in $\text{Mn}_{1/4}\text{NbS}_2$ is attributed to the position of the Fermi level which lies in between the opposite spin states of Mn. The larger size of the in-plane MAE, which is responsible for

the Ising spin state in $\text{Mn}_{1/4}\text{NbS}_2$, is due to the weakness or suppression of the positive term in overall MAE.

ACKNOWLEDGMENTS

This work was supported by the National Natural Science Foundation of China (Grants No. 12074360, No.

12074386, and No. 11874358), the Alliance of International Science Organizations (ANSO) (Grant No. ANSO-VF-2021-03), Anhui University Scientific Research Startup Fund (No. S020318006/023), the Key Project of Natural Scientific Research of Universities in Anhui Province (No. K120462009), and Anhui Provincial Natural Science Foundation No. 2108085QA21.

- [1] R. Friend and A. Yoffe, *Adv. Phys.* **36**, 1 (1987).
- [2] R. Friend, A. Beal, and A. Yoffe, *Philos. Mag.* **35**, 1269 (1977).
- [3] S. S. P. Parkin and R. H. Friend, *Philos. Mag. B* **41**, 65 (1980).
- [4] B. Van Laar, H. Rietveld, and D. Ijdo, *J. Solid State Chem.* **3**, 154 (1971).
- [5] H. Negishi, A. Shoube, H. Takahashi, Y. Ueda, M. Sasaki, and M. Inoue, *J. Magn. Magn. Mater.* **67**, 179 (1987).
- [6] A. Little, C. Lee, C. John, S. Doyle, E. Maniv, N. L. Nair, W. Chen, D. Rees, J. W. Venderbos, R. M. Fernandes *et al.*, *Nat. Mater.* **19**, 1062 (2020).
- [7] N. J. Ghimire, A. Botana, J. Jiang, J. Zhang, Y.-S. Chen, and J. Mitchell, *Nat. Commun.* **9**, 1 (2018).
- [8] T. Moriya and T. Miyadai, *Solid State Commun.* **42**, 209 (1982).
- [9] Y. Togawa, T. Koyama, K. Takayanagi, S. Mori, Y. Kousaka, J. Akimitsu, S. Nishihara, K. Inoue, A. Ovchinnikov, and J.-i. Kishine, *Phys. Rev. Lett* **108**, 107202 (2012).
- [10] H. Han, L. Zhang, D. Sapkota, N. Hao, L. Ling, H. Du, L. Pi, C. Zhang, D. G. Mandrus, and Y. Zhang, *Phys. Rev. B* **96**, 094439 (2017).
- [11] E. M. Clements, R. Das, L. Li, P. J. Lampen-Kelley, M.-H. Phan, V. Keppens, D. Mandrus, and H. Srikanth, *Sci. Rep.* **7**, 1 (2017).
- [12] Y. Dai, W. Liu, Y. Wang, J. Fan, L. Pi, L. Zhang, and Y. Zhang, *J. Condens. Matter Phys.* **31**, 195803 (2019).
- [13] C. Gong, L. Li, Z. Li, H. Ji, A. Stern, Y. Xia, T. Cao, W. Bao, C. Wang, Y. Wang *et al.*, *Nature (London)* **546**, 265 (2017).
- [14] B. hsHuang, G. Clark, E. Navarro-Moratalla, D. Klein, R. Cheng, K. Seyler, D. Zhong, E. Schmidgall, M. McGuire, D. Cobden *et al.*, *Nature (London)* **546**, 270 (2017).
- [15] Z. Fei, B. Huang, P. Malinowski, W. Wang, T. Song, J. Sanchez, W. Yao, D. Xiao, X. Zhu, A. F. May *et al.*, *Nat. Mater.* **17**, 778 (2018).
- [16] Y. Deng, Y. Yu, Y. Song, J. Zhang, N. Z. Wang, Z. Sun, Y. Yi, Y. Z. Wu, S. Wu, J. Zhu *et al.*, *Nature (London)* **563**, 94 (2018).
- [17] C. Zhang, Y. Yuan, M. Wang, P. Li, J. Zhang, Y. Wen, S. Zhou, and X.-X. Zhang, *Phys. Rev. Materials* **3**, 114403 (2019).
- [18] Y. Kuroiwa, M. Kunikata, and Y. Noda, *Mol. Cryst. Liq. Cryst. Sci. Technol., Sect. A* **341**, 87 (2000).
- [19] O. V. Dolomanov, L. J. Bourhis, R. J. Gildea, J. A. Howard, and H. Puschmann, *J. Appl. Crystallogr.* **42**, 339 (2009).
- [20] G. M. Sheldrick, *Acta Crystallogr.* **64**, 112 (2008).
- [21] G. M. Sheldrick, *Acta Crystallogr.* **71**, 3 (2015).
- [22] S. K. Karna, F. N. Womack, R. Chapai, D. P. Young, M. Marshall, W. Xie, D. Graf, Y. Wu, H. Cao, L. DeBeer-Schmitt, P. W. Adams, R. Jin, and J. F. DiTusa, *Phys. Rev. B* **100**, 184413 (2019).
- [23] S. Polesya, S. Mankovsky, H. Ebert, P. G. Naumov, M. A. ElGhazali, W. Schnelle, S. Medvedev, S. Mangelsen, and W. Bensch, *Phys. Rev. B* **102**, 174423 (2020).
- [24] A. Arrott, *Phys. Rev.* **108**, 1394 (1957).
- [25] S. Kaul, *J. Magn. Magn. Mater.* **53**, 5 (1985).
- [26] B. Banerjee, *Phys. Lett.* **12**, 16 (1964).
- [27] A. Arrott and J. E. Noakes, *Phys. Rev. Lett.* **19**, 786 (1967).
- [28] V. K. Pecharsky and K. A. Gschneidner, Jr., *J. Magn. Magn. Mater.* **200**, 44 (1999).
- [29] V. Franco, J. Blázquez, and A. Conde, *Appl. Phys. Lett.* **89**, 222512 (2006).
- [30] H. Stanley, *Introduction to Phase Transitions and Phenomena, Critical* (Clarendon Press, Oxford, 1971).
- [31] L. P. Kadanoff, *Phys. Phys. Fiz.* **2**, 263 (1966).
- [32] A. Rahman, M. u. Rehman, D. Zhang, M. Zhang, X. Wang, R. Dai, Z. Wang, X. Tao, L. Zhang, and Z. Zhang, *Phys. Rev. B* **100**, 214419 (2019).
- [33] H. E. Stanley, *Phase Transitions and Critical Phenomena* (Clarendon Press, Oxford, 1971).
- [34] M. Campostrini, M. Hasenbusch, A. Pelissetto, P. Rossi, and E. Vicari, *Phys. Rev. B* **65**, 144520 (2002).
- [35] J. C. Le Guillou and J. Zinn-Justin, *Phys. Rev. B* **21**, 3976 (1980).
- [36] S. J. Poon and J. Durand, *Phys. Rev. B* **16**, 316 (1977).
- [37] M. E. Fisher, S.-k. Ma, and B. Nickel, *Phys. Rev. Lett.* **29**, 917 (1972).
- [38] S. F. Fischer, S. N. Kaul, and H. Kronmüller, *Phys. Rev. B* **65**, 064443 (2002).
- [39] K.-T. Ko, K. Kim, S. B. Kim, H.-D. Kim, J.-Y. Kim, B. I. Min, J.-H. Park, F.-H. Chang, H.-J. Lin, A. Tanaka, and S.-W. Cheong, *Phys. Rev. Lett.* **107**, 247201 (2011).
- [40] G. Kresse and J. Furthmüller, *Phys. Rev. B* **54**, 11169 (1996).
- [41] S. Grimme, J. Antony, S. Ehrlich, and H. Krieg, *J. Chem. Phys.* **132**, 154104 (2010).
- [42] Z.-P. Shi, P. M. Levy, and J. L. Fry, *Phys. Rev. B* **49**, 15159 (1994).
- [43] S. Mankovsky, S. Polesya, H. Ebert, and W. Bensch, *Phys. Rev. B* **94**, 184430 (2016).